

# **Transport of Radon Gas into a Tunnel at Yucca Mountain—Estimating Large-Scale Fractured Tuff Hydraulic Properties and Implications on the Operation of the Ventilation System**

**<sup>†</sup>André Unger**

Earth Sciences Division  
Lawrence Berkeley National Laboratory  
One Cyclotron Road, MS 90-1116  
94720 USA  
[AJAUnger@lbl.gov](mailto:AJAUnger@lbl.gov)  
Phone: (510) 495-2823  
Fax: (510) 486-5686

**Stefan Finsterle**

Earth Sciences Division  
Lawrence Berkeley National Laboratory  
One Cyclotron Road, MS 90-1116  
94720 USA  
[SAFinsterle@lbl.gov](mailto:SAFinsterle@lbl.gov)  
Phone: (510) 486-5205  
Fax: (510) 486-5686

**Gudmundur Bodvarsson**

Earth Sciences Division  
Lawrence Berkeley National Laboratory  
One Cyclotron Road, MS 90-1116  
94720 USA  
[GSBodvarsson@lbl.gov](mailto:GSBodvarsson@lbl.gov)  
Phone: (510) 486-4789  
Fax: (510) 486-5686

<sup>†</sup>corresponding author

## Abstract

Radon gas concentrations have been monitored as part of the operation of a tunnel (the Exploratory Studies Facility—ESF) at Yucca Mountain to address regulatory issues regarding worker safety. The objective of this study was to examine the potential use of the radon data to estimate large-scale formation properties of fractured tuffs. This objective was examined by developing a numerical model based upon the characteristics of the ESF and the Topopah Spring welded (TSw) tuff unit capable of predicting radon concentrations for prescribed ventilation conditions. The model was used to address two specific issues. First, it was used to estimate the permeability and porosity of the fractures in the TSw at the length scale of the ESF and extending tens of meters into the TSw surrounding the ESF. Second, the model was used to understand the mechanism leading to radon concentrations exceeding the regulatory limit within the ESF. The mechanism controlling radon concentrations in the ESF is a function of atmospheric barometric fluctuations being propagated down the ESF along with the ventilated air flow in addition to the slight suction induced by the exhaust fans at the south portal of the ESF, causing the ventilation air flow. These pressure fluctuations are dampened in the TSw fracture continuum according to its permeability and porosity. Consequently, as the barometric pressure in the ESF drops rapidly, formation gases from the TSw are pulled into the ESF, resulting in high radon concentrations. Model calibration to both radon concentrations measured in the ESF, and gas-phase pressure fluctuations in the TSw yielded independent estimates of the TSw fracture permeability and porosity of  $1 \times 10^{-11} \text{ m}^2$  and 0.00034, respectively. The calibrated model was then used as a design tool to predict the effect of adjusting the current ventilation-system operation strategy for reducing the probability that radon gas concentrations will exceed the regulatory limit.

**Keywords** Yucca Mountain, radon, fracture permeability, fracture porosity, ventilation, inverse modeling

## Introduction

This study examines the potential use of radon concentration data to estimate large-scale formation properties of fractured tuffs. These tuffs are considered as the host rock for a potential repository of high-level nuclear waste to be located at Yucca Mountain, Nevada. Radon concentrations were available in the Exploratory Studies Facility (ESF), a large diameter tunnel partially excavated through Yucca Mountain. The ESF is 7857 m long, and was excavated to provide access to specific tuff units that were expected to impact the performance of the potential repository [Bodvarsson et al., 1999]. Access to the tunnel is through the north portal (see Figure 1), with the south portal used to permit exhaust fans to ventilate the ESF. These exhaust fans under pressurize the ESF relative to the atmosphere. The resulting suction causes atmospheric air to flow into the ESF for ventilation purposes, but also draws formation gases into the ESF that contain high levels of radon. Consequently, radon gas concentrations have been monitored as part of the operation of the ESF at Yucca Mountain. This monitoring ensures that workers are not exposed to concentrations of radon and its progeny in excess of the current 10 CFR Part 20 derived air concentration limit of  $1,110 \text{ Bq/m}^3$  (30 pCi/L) for radon and 0.33 WL for radon progeny [NRC, 1999]. In order to

examine the objective of this work, we developed a conceptual model followed by a numerical model based upon the characteristics of the ESF and the Topopah Spring welded (TSw) tuff unit capable of predicting radon concentrations for prescribed ventilation conditions. The TSw is important because it is the unit chosen to host the potential repository.

The fate and transport of radon in underground openings has received widespread attention due to the health risks associated with exposure to radon gas and its progeny. Przylibski [2001], Gillmore et al. [2000], Dueñas et al. [1999] and Tauahara et al. [1997] observed changes in the mean monthly radon concentrations in underground openings without effective ventilation. They attribute variations in the radon level to the correlation between the seasonal temperature of the atmospheric air relative to the formation temperature. The temperature difference provides a gradient in the potential of the gas phase (due to gas phase density) between the formation and the underground opening. Radon levels within the underground opening increase as formation gases flow from the formation into the underground opening and decrease as flow is reversed. In the case of the ESF at Yucca Mountain, active ventilation provides a gradient in the potential of the gas phase (due to gas phase pressure) between the formation and the ventilated air which is significantly greater than that which can be attributed to the temperature variations observed in underground openings without effective ventilation. The primary objective of this work involves using radon concentration data within the ESF observed during periods of active ventilation to estimate large-scale formation properties of fractured tuffs. As part of this work, we will not address issues related to the actual genesis of radon within the fractured tuffs, nor geochemical issues involving radon gas transport within the fractured tuffs surrounding the ESF. We will simply assume that radon is an ideal and inert gas tracer, has a constant ambient concentration, and is of unlimited supply within the unsaturated zone of Yucca Mountain. Brace [1980, 1984] and Clauser [1992] provide a comprehensive review of studies focused on determining the large-scale permeability of crystalline rocks, including a ventilation test performed within the Stripa mine [Wilson et al., 1983]. We believe our work further adds to this body of literature while including an independent porosity estimate.

Development of the conceptual model was based upon a review of available radon concentration data in the ESF, gas-phase pressure measurements within the ESF and adjacent TSw rock, and airflow rates down the ESF caused by ventilation. The numerical model, which followed from the conceptual model, was then used to achieve two goals. First, calibration of the model to existing radon concentration, pressure and ventilation rate data was used to estimate the permeability and porosity of the fractures in the TSw (on the scale of tens of meters) surrounding the ESF. These parameters were employed to corroborate values obtained from mountain-scale pneumatic pressure signals [Ahlers et al., 1999], air-injection tests in boreholes [Lecain, 1997; Freifeld, 2001], gas-tracer tests in boreholes [Freifeld, 2001] and geometric calculations of fracture aperture and spacing [Sonnenthal et al., 1997; Tsang and Birkholzer, 1999]. Second, the model was subsequently used to investigate the mechanism leading to radon concentrations in

excess of  $1,110 \text{ Bq/m}^3$  within the ESF. Once this mechanism was understood, the model then enabled us to predict the effect of adjusting the current operation strategy of the ventilation system on reducing the probability that radon gas concentrations would exceed  $1,110 \text{ Bq/m}^3$ . This design step was undertaken because extensive drift networks will need to be excavated and ventilated to emplace the waste, should the potential repository enter the engineering design and construction stage.

## Conceptual Model

The conceptual model is based on the hypothesis that atmospheric barometric–pressure fluctuations propagate down the ESF as air flows under reduced pressure (relative to the atmosphere) from the north portal towards the exhaust fans at the south portal. The amplitude of these barometric pressure fluctuations in the ESF is dampened as air flows into and out of the TSw. For instance, a rapid drop in barometric pressure within the ESF will cause a corresponding but dampened pressure drop within the TSw, causing formation gases to flow into the ESF and mix with the ventilated air. Conversely, a rapid rise in barometric pressure within the ESF will cause ventilated air from the ESF to flow into the TSw fracture network. Given that the ambient gas within the TSw contains high concentrations of radon, gas flow from the TSw into the ESF will cause a rise in radon concentrations within the ESF.

Development of the conceptual model was governed by available radon concentration and barometric pressure data within the ESF as well as gas–phase pressure data within the TSw fracture continuum. Radon concentration and barometric pressure data were collected at stations 34+86 and 50+35 located at 3486 *m* and 5035 *m* down the ESF from the north portal, respectively, over a 20 day time frame starting on July 22, 1999, and ending on August 10, 1999. The location of stations 34+86 and 50+35 is shown on Figure 1 while the radon and barometric pressure data are shown on Figure 2. Concurrent gas–phase pressure data were available at three separate locations in borehole NRG–7a (within the TSw) with sensor A located at the same elevation as the ESF, approximately 18 *m* into the TSw. Sensors B and C were located approximately 60 *m* and 100 *m* above sensor A, respectively. All three sensors measured gas–phase pressure fluctuations in the TSw fracture continuum. As shown on Figure 1, the position of borehole NRG–7a is upstream of the interval bounded by stations 34+86 and 50+35, given the airflow direction. Despite the upstream location of NRG–7a, gas–phase pressure fluctuations within the borehole were taken to be representative of ambient gas–phase pressure conditions within the TSw, between 3,486 *m* and 5,035 *m* down the ESF. This geometric simplification in the conceptual model is based on the assumption that the large–scale permeability and porosity of the TSw are constant over this distance. The interval bounded by stations 34+86 and 50+35 was also selected because the ESF is located within the TSw in this section.

Based upon radon concentrations of  $65,000 \text{ Bq/m}^3$  measured in Alcove 7 (see Figure 2) between February 7, 1999, and February 17, 1999, when the bulkhead to the alcove was sealed (as indicated by humidity levels near 100%), the ambient radon concentration within the TSw is expected to be on the order of

100,000  $Bq/m^3$  (given mixing and dilution within Alcove 7). The ambient TSw radon concentration is quickly diluted as it is mixed with ventilated air within the ESF, down to a maximum value of 2204  $Bq/m^3$  (as shown on Figure 2). Despite the dilution, radon concentration levels frequently exceeded the regulatory limit of 1,110  $Bq/m^3$  over the 20 day period shown in Figure 2.

Figure 3 shows point measurements of ventilation airflow velocity averaged at ESF stations 28+93 and 51+84 during the period from July 22, 1999, to August 10, 1999 [Flint, 1999]. The interval between these stations bounds the section of the ESF used to define the conceptual model. Airflow velocity remained relatively constant at both stations, with a mean value of 2.0  $m/s$  and a minimum and maximum value of 1.7  $m/s$  and 2.2  $m/s$ , respectively. Given that the radius of the ESF is 3.81  $m$ , the mean ventilation rate was estimated as 91  $m^3/s$ , with a minimum and maximum value of 78  $m^3/s$  and 100  $m^3/s$ , respectively. The regularity at which the air velocity fluctuates between 1.7  $m/s$  and 2.2  $m/s$  is a consequence of whether one or two exhaust fans are used to ventilate the ESF. There appears to be a distinct correlation between the radon peaks and when the second fan is turned on, increasing the air velocity. Presumably, this also results in increased suction, drawing a pulse of formation gases into the ESF. Note that the conceptual model makes no assumptions about this relationship because the pressure data used within the conceptual model will capture this effect.

We assumed the system was isothermal and at 23°C which is the ambient temperature of the TSw at the elevation of the ESF. The temperature of air within the ESF did fluctuate over the twenty day period, but remained close to that of the TSw. Therefore, it was also assumed to remain constant at 23°C for the purposes of this study. Humidity variations between the gas phase in the TSw and that in the ESF were assumed not to influence either advection of the gas phase or transport of radon within the gas phase. These assumptions follow from the conceptual model which is based on the hypothesis that advection of the gas phase is driven by barometric fluctuations resulting in gas phase pressure differences between the ESF and TSw. Gas phase potential differences between the ESF and TSw as influenced by temperature and humidity variations are assumed to be of secondary importance.

## **Numerical Model**

A numerical model was developed using the flow and transport code TOUGH2 EOS7r [Pruess, 1991; Oldenburg and Pruess, 1995]. A detailed description of all physical processes and resulting equations within TOUGH2 EOS7r is given by Oldenburg and Pruess [1995] and will not be repeated here for brevity. The physical processes relevant to the conceptual and numerical model presented here involve a two phase gas/water system where the water is immobile (at residual saturation) within the TSw fracture continuum and nonexistent within the ESF, while the gas phase is mobile within both the TSw fracture continuum and ESF. Three components exist within the conceptual and numerical models and are air, water and radon ( $^{222}\text{Rn}$ ). All three components can partition into the two phases. Given that the gas phase is the only mobile

phase, advection of the three components only occurs in the gas phase although diffusion occurs in both the gas and water phases. As radon is transported within the ESF and TSw fracture continuum, it decays, with a half-life of 3.823 days.

The numerical model was developed in cylindrical coordinates, with the length (Cartesian) axis oriented along the ESF and the radial axis from the center of the ESF into the TSw. The model was 1549 *m* in length (between stations 34+86 and 50+35—see Figure 1) and with an outer radius of 66.45 *m*. The radius of the model was chosen to be equal to the radial distance where sensor B of borehole NRG-7a is from the center of the ESF. NRG-7a sensor B was chosen to define the perimeter of the model, because barometric pressure fluctuations within the ESF did not interfere with either NRG-7a sensor B or C, which exhibit identical pressure fluctuations. Gas-phase pressure fluctuations in NRG-7a sensors B and C represent the mountain-scale atmospheric barometric signal propagating through the TSw.

Figure 4 shows the mesh used in the numerical model, which consists of 3 nodes along the length axis, used to represent air flow down the ESF, and 50 nodes along the radial axis of the model, used to resolve gas-phase flow and radon transport between the TSw and ESF. Note that the TSw boundary node, the ESF entrance boundary node, and the ESF exit boundary node, as shown on Figure 4, serve as locations for specifying boundary conditions as described below. The dimension of the ESF node along the length axis is 1549 *m* to represent the distance between stations 34+86 and 50+35. All features which intersect the ESF between these stations such as Niches 1, 2 and 4, the Sundance Fault, Alcove 6, and the Ghost Dance Fault which intersects Alcove 6 (as shown on Figure 1) are lumped into the single ESF node. Boundary conditions include specifying gas-phase pressure along the radial perimeter of the model (TSw boundary node) following the gas-phase pressure fluctuations shown by NRG-7a sensor B on Figure 2. The radon concentration along the perimeter was taken to be constant and represents the ambient mountain-scale radon concentration in the TSw. Gas-phase pressures at the exit boundary node of the ESF followed the barometric fluctuations shown by ESF 50+35 on Figure 2. Air was injected in the entrance boundary node of the ESF at a ventilation rate obtained by multiplying the airflow velocity data shown on Figure 3 by the cross-sectional area of the ESF. The radon concentration of the injected gas phase (ventilated air) following the signal shown by ESF 34+86 on Figure 2.

The model is essentially one-dimensional, involving transient radial flow of air and transport of radon in the TSw as well as uniform mixing of the formation gas with the ventilated air in the ESF. The geometric simplification of the model was based upon the observation that the rate of ventilated air flushes the entire volume between ESF 34+86 and 50+35 every twenty minutes whereas the wavelength of the radon peaks shown on Figure 2 are on the order of one-half day. Therefore, the ESF was conceptualized as a simple mixing volume rather than a long tube requiring multiple nodes to discretize and resolve flow and transport along its length. The accuracy of this assumption was verified by comparing radon concentrations at ESF

50+35, using a variation of the model where the Cartesian axis (including the ESF and TSw) was discretized into 100 nodes. Both models yielded identical results, with the computational burden of the latter being orders of magnitude greater. Nodes comprising the TSw represented a single fracture continuum with a water saturation of 0.05. Nodes comprising the ESF were assigned an artificially high permeability of  $1 \times 10^{-2} \text{ m}^2$  to limit the pressure gradient along the ESF while maintaining smooth convergence of the Newton iteration within TOUGH2.

## Model Calibration

Calibration of the numerical model was performed using iTOUGH2 [Finsterle, 1999] with the Levenberg–Marquardt algorithm. Calibration targets included the NRG–7a sensor A gas–phase pressure and ESF 50+35 radon concentration data sets. Calibration was performed on data from day 2 (July 22, 1999) to day 10 (July 31, 1999), while data from day 10 to day 20 (August 10, 1999) were used for testing the predictive capabilities of the calibrated model. To calibrate to these data sets, six parameters controlling the behavior of the physical model were estimated by iTOUGH2. These were the permeability and porosity of the TSw fracture continuum, the ambient radon concentration in the TSw, an independent pressure shift for both the NRG–7a sensor A and B gas–phase pressure data, and ventilation rate. Here, we assumed that the datum of the ESF 50+35 pressure transducer is known reliably well, whereas the datum for the NRG–7a transducers is unknown. The pressure shift also automatically corrects these data sets for a static gravity potential, so that they are evaluated at the same elevation in the physical model as ESF 50+35. The ventilation rate was estimated because of the difficulty in calculating the ventilation rate based upon point measurements of air velocity. *A priori* estimates of ventilation rate were based on multiplying the air velocity data by the cross-sectional area of the ESF, with the mean ventilation rate equal to  $91 \text{ m}^3/\text{s}$ .

Figure 5 shows the measured, calibrated and predicted pressure signals at NRG–7a sensor A and the radon concentration signal at ESF 50+35. Examination of the calibrated and predicted gas–phase pressure signal shows an accurate fit to the measured data. The calibrated and predicted radon signal also shows an accurate fit with the greatest deviation occurring during the radon peaks when the greatest pressure differential occurs between the TSw and ESF and flow of formation gases into the ESF is greatest. Specifically, an *a priori* mean error of  $20 \text{ Pa}$  was assumed for the gas–pressure data residuals, with the *posteriori* mean residual equal to  $13 \text{ Pa}$ . In addition, an *a priori* mean error of  $100 \text{ Bq/m}^3$  was assumed for the radon data, with the *posteriori* mean error calculated as  $74 \text{ Bq/m}^3$ . The *a priori* mean errors were assumed because actual values were not provided with the data sets. Our choice of values was based on our intent to weight the radon and pressure data equally during the inversion. At the minimum of the objective function, which provides the best–fit parameter set for the radon and pressure data, the pressure data contributed to 44% of its value, while the radon data contributed to 56% of its value. The upper and lower 95% confidence bounds were obtained using linear uncertainty propagation analysis. These results show

that the simulated radon concentrations are significantly more sensitive to parameter uncertainty than the simulated pneumatic pressures.

In general, flow of air is from the TSw into the ESF, owing to the slight pressure drop induced by the exhaust fans at the south portal. The pressure drop was calculated to be on average 154  $Pa$  at ESF 50+35 over the 20 day simulation period. Flow reversals occur at 6, 10.25, 11, 15.25, 19.25, and 20 days, as shown in Figure 2. These flow reversals are of short duration and characterized by low radon concentrations in the ESF (equal to the upstream concentration at ESF 34+86), which get pushed approximately 10 meters into the TSw. The highest radon concentration occurred at 13.75 days and was driven by a pressure differential of 436  $Pa$  between NRG-7a sensor B and ESF 50+35. This peak was followed by a flow reversal at 15.25 days, which was driven by a pressure differential of 18  $Pa$  between ESF 50+35 and NRG-7a sensor B.

The mean value and standard deviations for the six estimated parameters, as well as a matrix of direct correlations between pairs of parameters is provided on Tables 1 and 2, respectively. Analysis of these results indicates that the TSw permeability and porosity are relatively strongly correlated, as expected, given their combined role in propagating transient pressure fluctuations between the ESF and TSw. This relationship is expressed as the “gas diffusivity” and is calculated as the ratio of the permeability times the ambient gas-phase pressure ( $\sim 88$   $kPa$ ) to the porosity times the gas viscosity ( $\sim 1.8 \times 10^{-5}$   $Pa \cdot s$ ) [Ahlers et al., 1999]. The TSw permeability, ambient TSw radon concentration, and ventilation rate are highly correlated, suggesting the model is over parameterized and pointing to the possible non uniqueness of the calibrated parameter set. This is reflected in the large standard deviations of the ambient TSw radon concentration and ventilation rate. The strong correlation between these parameters is supportive of the physical model representing a relatively simple mixing problem, in which radon from the TSw is diluted by the ventilated air in the ESF. In this case, it is not reasonable to estimate the permeability of the TSw, which controls the darcy flux of the gas phase through the TSw as well as the ambient radon concentration in the TSw, with the two multiplied together yielding the mass flux of radon into the ESF. Independent measurement of the ambient radon concentration in the TSw is required to uniquely determine the TSw permeability and porosity. Finally, the ventilation rate was increased by a factor of 1.4 relative to the *a priori* mean ventilation rate during model calibration by iTOUGH2. This scaling underlies the difficulty in estimating the ventilation rate from point measurements of air velocity. Ideally, this model calibration exercise should be restricted to estimating the permeability and porosity of the TSw with *a priori* estimates of ambient TSw radon concentration, the datum of the pressure transducers, and the ventilation rate known to a high degree of accuracy. Incomplete knowledge of these parameters represents data gaps in the conceptual model.



A unique contribution from the joint inversion of the gas–phase pressure and radon data is the independent estimation of the TSw fracture permeability and porosity. This is shown on Figure 6 which provides contours of the objective function as a function of permeability and porosity when (a) both radon and pressure data are considered, (b) only pressure data are included, and (c) only radon data are used for the inversion. These results show that the objective function is primarily determined from radon data residuals and is significantly less sensitive to the pressure data residuals. In particular, the minimum of the objective function indicates that uncertainty in the range of the permeability estimate is very small (from  $10^{-11.1}$  to  $10^{-10.9} \text{ m}^2$ ) whereas uncertainty on the range of the porosity estimate is large (from  $10^{-4}$  to  $10^{-2.5}$ ). When only pressure data are considered, the objective function yields a line of minima, indicating that permeability and porosity cannot be uniquely determined. The slope of these minima yields a gas diffusivity of  $0.2 \text{ m}^2/\text{s}$ , which is consistent with the value Ahlers et al. [1999] determined for the TSw fractures. The minimum obtained from the joint inversion of the radon and pressure data yields a gas diffusivity of  $140 \text{ m}^2/\text{s}$ , which is within the range of fault values determined by Ahlers et al. [1999]. However, we do not conclude that radon concentrations within the section of ESF represented in the conceptual model are controlled by transport from fault intersections with the ESF. These fault intersections would include the Sundance Fault as well as the Ghost Dance Fault, which crosses Alcove 6. Note that borehole NRG–7a sensors A, B and C record gas–phase pressure fluctuations in the TSw fracture continuum and are not influenced by either the Sundance or Ghost Dance Faults. Our reasoning is that transport of radon in the conceptual model (representing the TSw fracture continuum only) is controlled by the suction induced by the exhaust fans at the south portal, as well as the difference in the amplitude of pressure fluctuations occurring between NRG–7a sensor B, which represents the boundary of the model, and ESF 50+35. Therefore, although the radon data suggest the system may be fault controlled, the pressure data representing the boundary condition driving transport indicate the system is fracture controlled. This is also supported by the very small standard deviation in the pressure shift estimated for the NRG–7a sensor B data (see Table 1) and the fact that the conceptual model is able to match both the pressure and radon data, as indicated by the small *posteriori* residual errors. If transport of radon was largely fault controlled, then our conceptual model would not be able to provide an adequate fit to the radon and pressure data unless the mountain–scale atmospheric barometric signal propagating through the TSw fracture continuum were identical to that of the faults intersecting the ESF. By analyzing their different mountain–scale atmospheric barometric signals, Ahlers et al. [1999] determined that these faults have significantly different gas diffusivities than the TSw fracture continuum.

We hypothesize that the difference between the best–estimate parameter set derived from the radon and pressure data results from the transport of radon being preferentially channeled in the larger–aperture kinematically–connected fractures. This subset of fractures would have a higher permeability and smaller porosity relative to the total network of fractures in the TSw. Dissipation of pressure fluctuations on account of the gas diffusivity occurs in all of the connected fractures in the TSw fracture network,

including dead-end fractures that do not participate in the transport of radon. This yields a lower net permeability and higher porosity. In general, the estimated permeability of the TSw fracture continuum obtained from the radon data is one to four orders of magnitude larger than values obtained from borehole air-injection tests conducted by Lecain [1997] and Freifeld [2001]. This can be attributed to the scale difference between the radon and the air-injection data, as well as to heterogeneity in the properties of the TSw fracture continuum. The estimated porosity of the TSw fracture continuum is an order of magnitude smaller than values measured by Freifeld [2001] using gas-tracer tests in boreholes. This difference is not unreasonable given that the radon data were fairly insensitive to the fracture porosity over this range. This is characterized by the standard deviation of porosity from Table 1, where the mean plus three standard deviations yields a porosity estimate which is an order of magnitude greater than the mean. The estimated porosity is slightly larger than values obtained from geometric calculations of fracture aperture and spacing [Sonnenthal et al., 1997; Tsang and Birkholzer, 1999].

### **Interpretation of Experimental Data for Ventilation System Design**

The premise of the ventilation system design is to minimize the probability that radon concentrations will exceed the current 10 CFR Part 20 derived air concentration limit of  $1,110 \text{ Bq/m}^3$  of radon at any position within the ESF. This could easily be achieved by over pressurizing the ESF relative to the TSw by reversing the fans at the south portal. This would ensure that radon-free atmospheric air is continually lost to the TSw and subsequently replaced by the ventilation system. In this study, we assume that the current method of under pressurizing the ESF will be continued during the engineering design and construction stage of the Yucca Mountain Project.

The difference in radon concentration levels between ESF 34+86 and ESF 50+35 shown on Figure 2 can be interpreted as the gain in radon along a  $1,549 \text{ m}$  section of the ESF, given a stochastic barometric pressure signal caused by atmospheric conditions. Assuming a deterministic TSw fracture permeability, porosity, ambient radon concentration, and ventilation rate, ESF 34+86 has a probability of 0.06 that radon concentration will exceed  $1,110 \text{ Bq/m}^3$  of radon over the 20 day observation period shown on Figure 2. At the downstream end of the section at ESF 50+35, the probability of exceedence increases to 0.22, reflecting the gain of radon over the  $1,549 \text{ m}$  length of the ESF. Note that we assume that the observed pressure fluctuations over the 20 day observation period are a stationary realization of the general, stochastic barometric signal.

The calibrated model was used as a ventilation system design tool by calculating the required ventilation rate needed to reduce the probability that radon concentrations will exceed  $1,110 \text{ Bq/m}^3$  at a given position along the ESF. This methodology is demonstrated in Figures 7 and 8, which show the predicted probability of exceedence for Alcove 7 located at ESF 50+64 for three different ventilation rates. The rates are  $127 \text{ m}^3/\text{s}$  (which was obtained from the calibrated model)  $254 \text{ m}^3/\text{s}$ , and  $64 \text{ m}^3/\text{s}$ , with the latter two rates

obtained by doubling and halving the calibrated rate, respectively. The gain in radon concentration per meter of ESF, as shown in Figure 7, was calculated by prescribing a zero radon concentration at the ESF entrance boundary node. Furthermore, the pressure differential between the ambient atmospheric pressure, both outside the north portal (and within the TSw) and ESF 50+35 of 154 *Pa* was doubled as the ventilation rate was doubled. Conversely, the pressure differential was halved as the ventilation rate was halved. Therefore, we assumed that the pressure differential was proportional to the ventilation rate. Finally, the simulated gain in radon concentration was divided by the 1549 *m* length of the ESF section used in the calibrated model to yield the radon gain per meter of ESF. Over the twenty-day observation period shown on Figure 8, the predicted probability of exceedence for Alcove 7, located at ESF 50+64, was then calculated by scaling the radon gain per meter of the ESF by a factor of 5,064. The validity of this procedure was verified by checking that scaling the radon gain per meter of ESF could reproduce the observed radon concentration at ESF 34+86 and ESF 50+35. Specifically, at ESF 34+86 and 50+35, the radon-gain method yielded reasonable predictions of radon concentration that were on average a factor of 1.16 and 1.21 greater, respectively, than the recorded data. The probability of exceedence at ESF 34+86 and 50+35 calculated using the radon gain method was 0.08 and 0.26, respectively, which were also slightly greater than the recorded data.

The probability of exceedence is shown on Figure 8 as a function of uncertainty in the TSw fracture permeability and ambient radon concentration. The TSw fracture porosity is not shown because it was a relatively insensitive parameter. The box defines the 95% confidence interval for the estimated permeability and ambient radon concentrations, with the lower limit fixed at 65,000 *Bq/m<sup>3</sup>* (based on the Alcove 7 concentration data). Model results indicate that as the ventilation rate is increased from 64 *m<sup>3</sup>/s*, 127 *m<sup>3</sup>/s* to 254 *m<sup>3</sup>/s*, the probability of exceedence at Alcove 7 decreases from 0.30, 0.26 to 0.12, respectively. This implies that the benefits of dilution on reducing overall radon concentrations due to an increase in ventilation rate outweigh the increase in formation gases pulled into the ESF as the pressure differential between the ESF and TSw is increased. Unfortunately, the probability of exceedence increases dramatically for the higher ventilation rates, as the TSw fracture permeability and ambient radon concentration deviate above the mean estimated values. This results from combining the increased suction required to achieve the higher ventilation rates, with either increased permeability of ambient radon concentration yielding a larger mass flux of radon in the ESF. This increase in the mass flux of radon then causes a corresponding increase in the probability of exceedence.

## Summary and Conclusions

A preliminary conceptual and numerical model was developed from available radon concentration measurements in the ventilated air within the ESF as well as barometric pressure fluctuations within the ESF and TSw fracture continuum. The model was based upon the hypothesis that atmospheric barometric fluctuations get propagated down the ESF as air flows from the north portal to the exhaust fans at the south

portal. The amplitudes of these barometric fluctuations are dampened as air flows through the TSw. A rapid drop in barometric pressure within the ESF will cause formation air to flow into the ESF, mixing with the ventilated air. Conversely, a rapid rise in barometric pressure within the ESF will cause ventilated air in the ESF to flow into the TSw. Given that the ambient gas within the TSw contains high concentrations of radon, gas flow from the TSw into the ESF will cause a rise in radon concentrations within the ESF. Calibration of the numerical model to the available data confirmed the hypothesis regarding the mechanism controlling radon concentrations within the ESF. Data gaps caused non-uniqueness issues regarding calibrated parameter values, resulting in relatively large standard deviations for some of the estimated values. In general, joint inversion of the radon data collected in the ESF and gas-phase pressure data from borehole NRG-7a sensor A yielded independent estimates of the TSw fracture permeability and porosity on the scale of tens of meters surrounding the ESF. The estimated values for the TSw fracture permeability and porosity are  $1 \times 10^{-11} \text{ m}^2$  and 0.00034, respectively. Furthermore, the radon data suggest that transport of radon is preferentially focused within the larger aperture fractures, yielding a higher permeability and lower porosity relative to values obtained from the pressure data only.

Radon levels within the ESF periodically exceed the current 10 CFR Part 20 derived air concentration limit of  $1,110 \text{ Bq/m}^3$  because of the current operation strategy of the ventilation system. We define the term “probability of exceedence” to indicate the fractional time that radon concentrations exceed the regulatory limit. The probability of exceedence increases along the length of the ESF, from the north to the south portal where the exhaust fans are located, due to the gain of radon from the formation. The calibrated model was used as a design tool to predict the effect of adjusting the current operation strategy of the ventilation system on reducing the probability of exceedence at Alcove 7. Model results indicate that as the ventilation rate is increased from  $64 \text{ m}^3/\text{s}$ ,  $127 \text{ m}^3/\text{s}$  to  $254 \text{ m}^3/\text{s}$ , the probability of exceedence at Alcove 7 decreases from 0.30, 0.26 to 0.12, respectively. This implies that the benefits of dilution on reducing overall radon concentrations caused by an increase in ventilation rate outweigh the increase in formation gases pulled into the ESF as the pressure differential between the ESF and TSw is increased. Unfortunately, the probability of exceedence increases dramatically for the higher ventilation rates, as the TSw fracture permeability and ambient radon concentration deviate above the mean estimated values. This results from the combination of the increased suction required to achieve the higher ventilation rates, with either increased permeability or ambient radon concentration, yielding a larger mass flux of radon in the ESF. This increase in the mass flux of radon then causes a corresponding increase in the probability of exceedence.

## Acknowledgements

The authors would like to thank Barry Freifeld, Rick Ahlers, Dan Hawkes, Stephanie Somot and Kent Novakowski for their review of the manuscript. The authors would also like to thank Bill Carl for providing the ESF radon and pressure data. This work was supported by the Director, Office of Civilian Radioactive

Waste Management, U.S. Department of Energy, through Memorandum Purchase Order EA9013MC5X between Bechtel SAIC Company, LLC and the Ernest Orlando Lawrence Berkeley National Laboratory (Berkeley Lab). The support is provided to Berkeley Lab through the U.S. Department of Energy Contract No. DE-AC03-76SF00098.

## References

- Ahlers, C.F., S. Finsterle, and G.S. Bodvarsson, 1999. Characterization and prediction of subsurface pneumatic response at Yucca Mountain, Nevada, *Journal of Contaminant Hydrology*, 38, 47–68.
- Bandurraga, T.M. and G.S. Bodvarsson, 1999. Calibrating hydrogeologic parameters for the 3–D site–scale unsaturated zone model of Yucca Mountain, Nevada. *Journal of Contaminant Hydrology*, 38, 25–46.
- Bodvarsson, G.S., W. Boyle, R. Patterson and D. Williams, 1999. Overview of scientific investigations at Yucca Mountain—the potential repository for high–level nuclear waste, *Journal of Contaminant Hydrology*, 38, 3–24.
- Brace, W.F., 1980. Permeability of crystalline and argillaceous rocks., *Int. J. Rock Mech. Min. Sci. and Geomech. Abstr.*, 17, 241.
- Brace, W.F., 1984. Permeability of crystalline rocks: new in situ measurements., *J. Geophys. Res.*, 89(B6), 4327.
- Clauser, C., 1992. Permeability of crystalline rocks. *EOS, Transactions, American Geophysical Union*, 73(21), May 26, 237.
- Dueñas, C., M.C. Fernández, S. Cañete, J. Carretero and E. Liger, 1999.  $^{222}\text{Rn}$  concentrations, natural flow rate and the radiation exposure levels in the Nerja Cave. *Atmospheric Environment*, 33, 501–510.
- Finsterle, S., 1999. ITOUGH2 User’s Guide, Rep. LBNL–40040, Lawrence Berkeley National Laboratory, Berkeley, CA.
- Flint, A.L., 1999. *Moisture monitoring in the ESF*, 12/98–7/99 (DTN:GS990908312242.011), Las Vegas, Nevada: CRWMS M&O.
- Freifeld, B.M., 2001. Estimation of fracture porosity in an unsaturated fractured welded tuff using gas tracer testing, Ph.D. Thesis: Department of Civil and Environmental Engineering, University of California, Berkeley, Fall 2001.
- Gillmore, G.K., M. Sperrin, P. Phillips, A. Denman, 2000. Radon hazards, geology, and exposure of cave users: a case study and some theoretical perspectives., *Ecotoxicology and Environmental Safety*, 46(3), 279–288.
- Lecain, G.D., 1997. Air–injection testing in vertical boreholes in welded and nonwelded tuff, Yucca Mountain, Nevada, *U.S. Geological Survey Water–Resources Investigations Report 96–4262*, GS960908312232.012 (non–Q), GS960908312232.013 (Q). U.S. Geological Survey, Denver, CO.
- NRC (US Nuclear Regulatory Commission), 1999. *10 CFR 20. Energy: Standards for protection against radiation*. Washington D.C.: US NRC.

- Oldenburg, C.M. and K. Pruess, 1995. EOS7R: Radionuclide transport for TOUGH2, Rep. LBL-34868, Lawrence Berkeley Laboratory, Berkeley, CA.
- Pruess, K., 1991. TOUGH2—A general-purpose numerical simulator for multiphase fluid and heat flow, Rep. LBL-29400, Lawrence Berkeley Laboratory, Berkeley, CA.
- Przylibski, T.A., 2001. Radon and its daughter products behaviour in the air of an underground tourist route in the former arsenic and gold mine in Zloty Stok (Sudety Mountains, SW Poland)., *Journal of Environmental Radioactivity*, 57(2), 87–103.
- Sonnenthal, E.L., C.F. Ahlers and G.S. Bodvarsson., 1997. Fracture and fault properties for the UZ site-scale flow model, Chapter 7 in *The Site-Scale Unsaturated Zone Model of Yucca Mountain, Nevada, for the Viability Assessment*, Report LBNL-40376, Lawrence Berkeley National Laboratory, Berkeley, CA.
- Tanahara, A., H. Taira and M. Takemura, 1997. Radon distribution and the ventilation of a limestone cave on Okinawa., *Geochemical Journal*, 31(1), 49–56.
- Tsang, Y.W., and J.T. Birkholzer, 1999. Predictions and observations of the thermal-hydrological conditions in the Single Heater Test, *Journal of Contaminant Hydrology*, 38, 385–425.
- Wilson, C.R., P.A. Witherspoon, J.C.S. Long, R.M. Galbraith, A.O. DuBois and M.J. McPherson, 1983., Large scale hydraulic conductivity measurements in fractured granite., *Int. J. Rock Mech. Min. Sci. and Geomech. Abstr.*, 20(6), 269.

Table 1: Mean and standard deviations for the six estimated parameters in the physical model.

<b>Estimated Parameter</b>	<b>Mean</b>	<b>Standard Deviation</b>
TSw fracture permeability	$1.0 \times 10^{-11} m^2$	$0.123 \log_{10}\{m^2\}$
TSw fracture porosity,	0.00034	$0.272 \log_{10}\{-\}$
Ambient TSw radon concentration	$110,000 Bq/m^3$	$28,000 Bq/m^3$
Pressure shift for NRG-7a sensor A	$-260.0 Pa$	$3.27 Pa$
Pressure shift for NRG-7a sensor B	$346.0 Pa$	$5.17 Pa$
Rate of ventilated air (mean value)	$127 m^3/s$	$26.5 m^3/s$

Table 2: Matrix of direct correlations for the six estimated parameters in the physical model

	<b>permeability</b>	<b>porosity</b>	<b>Radon conc.</b>	<b>sensor A</b>	<b>sensor B</b>	<b>vent. rate</b>
<b>permeability</b>	1.0	0.891	-0.997	0.0	-0.445	0.996
<b>porosity</b>	0.891	1.0	0.882	-0.006	0.409	-0.885
<b>radon conc.</b>	-0.997	0.882	1.0	0.0	-0.443	0.995
<b>sensor A</b>	0.0	-0.006	0.0	1.0	-0.850	0.0
<b>sensor B</b>	-0.445	0.409	-0.443	-0.850	1.0	0.443
<b>vent. rate</b>	0.996	-0.885	0.995	0.0	0.443	1.0

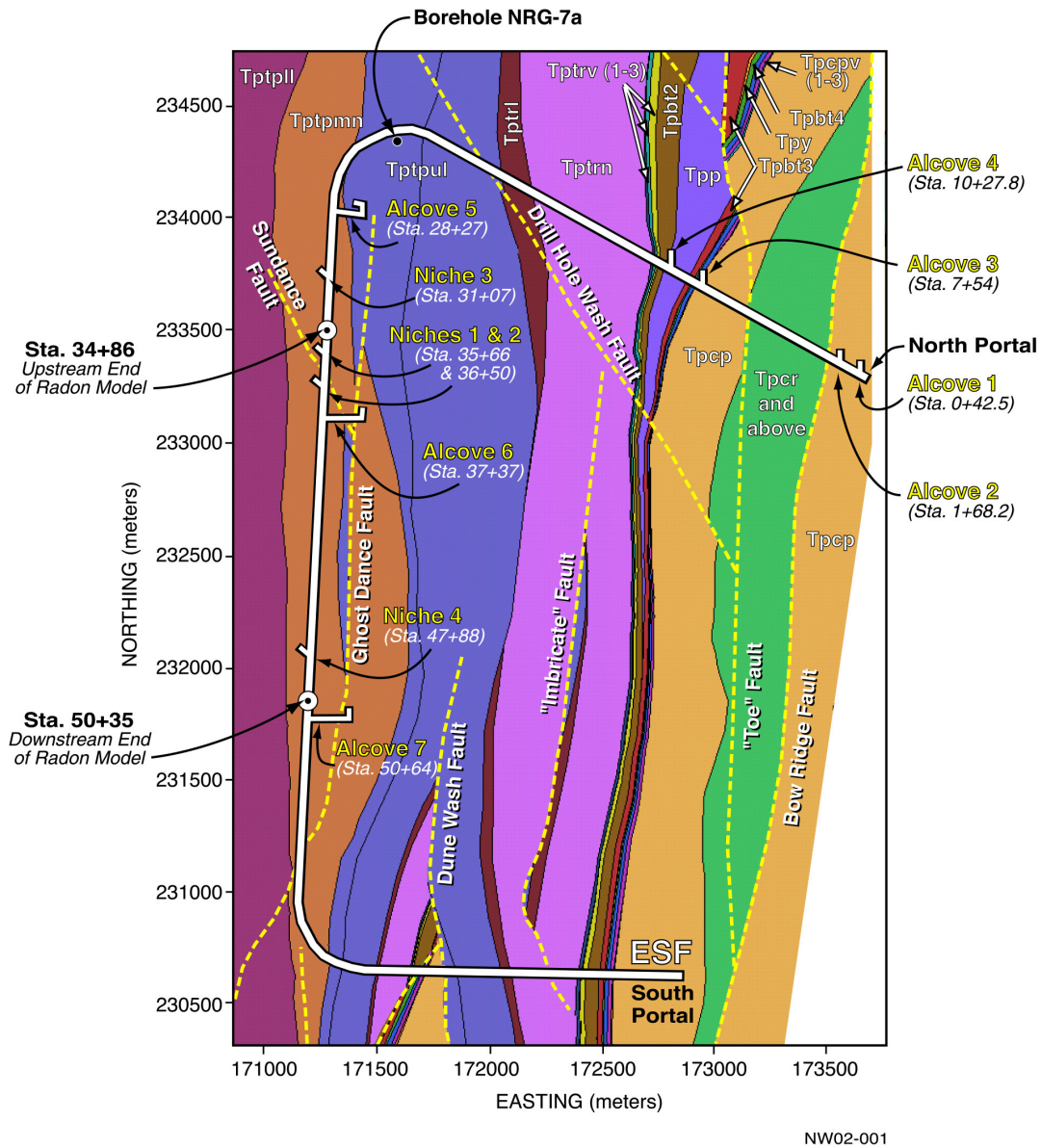


Figure 1. Location map of the ESW. The section of the ESW comprising the conceptual model is denoted by the arrows pointing to the upstream and downstream ends of the radon model (ESW stations 34+86 to 50+35). The TSw consists of the following subunits: Tptpl, Tptpmn, Tptpul, Tptrl, Tptrn, Tptrv (1–3) as described by Bandurraga and Bodvarsson [1999].



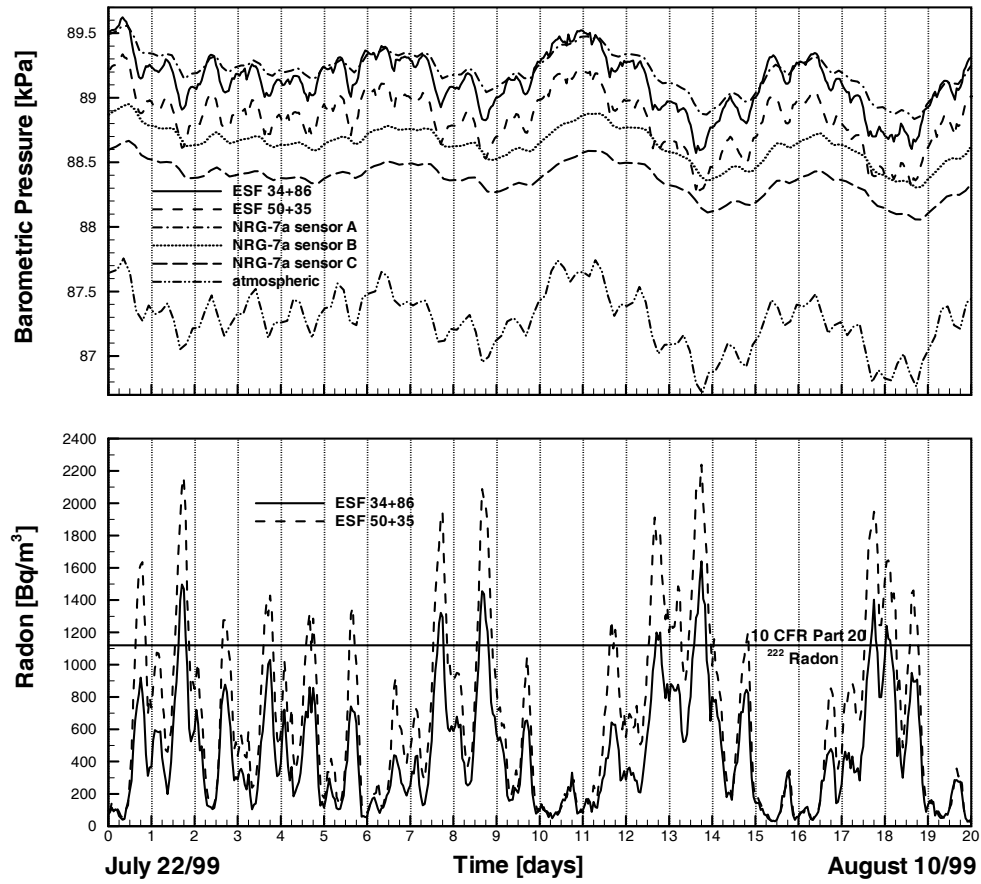


Figure 2. Barometric pressure data within the ESF, TSw gas-phase pressure data from borehole NRG-7a, as well as radon concentration measurements within the ESF.

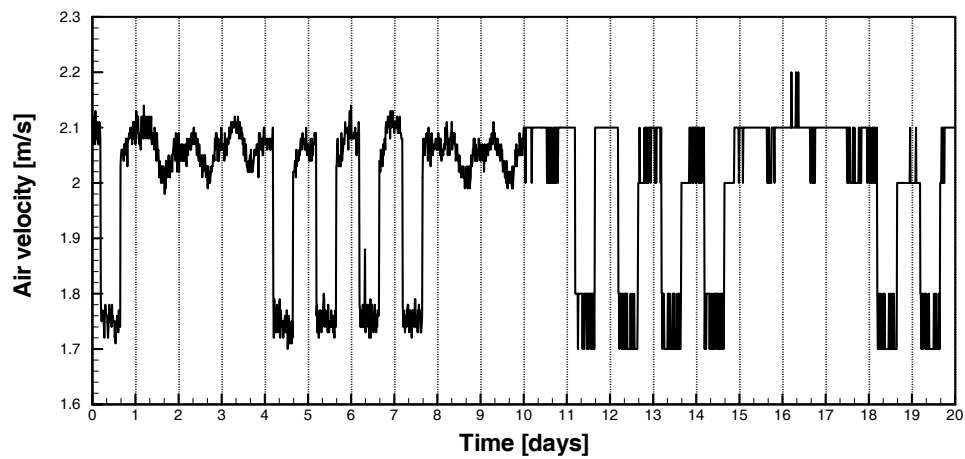


Figure 3. Air velocity data

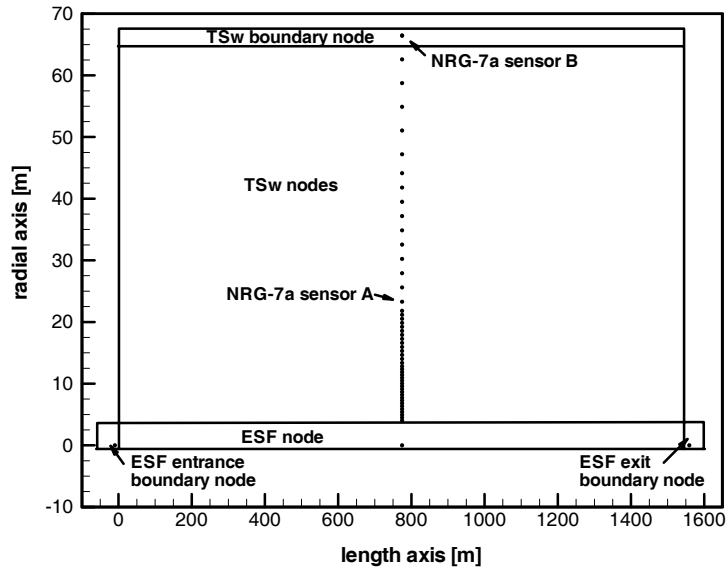


Figure 4. Plan view of mesh used in the numerical model. Dots represent the centroids of the control volume elements. The radial spacing between nodes within the TSw increases from 0.46 m, 0.65 m, 2.32 m to 3.85 m.

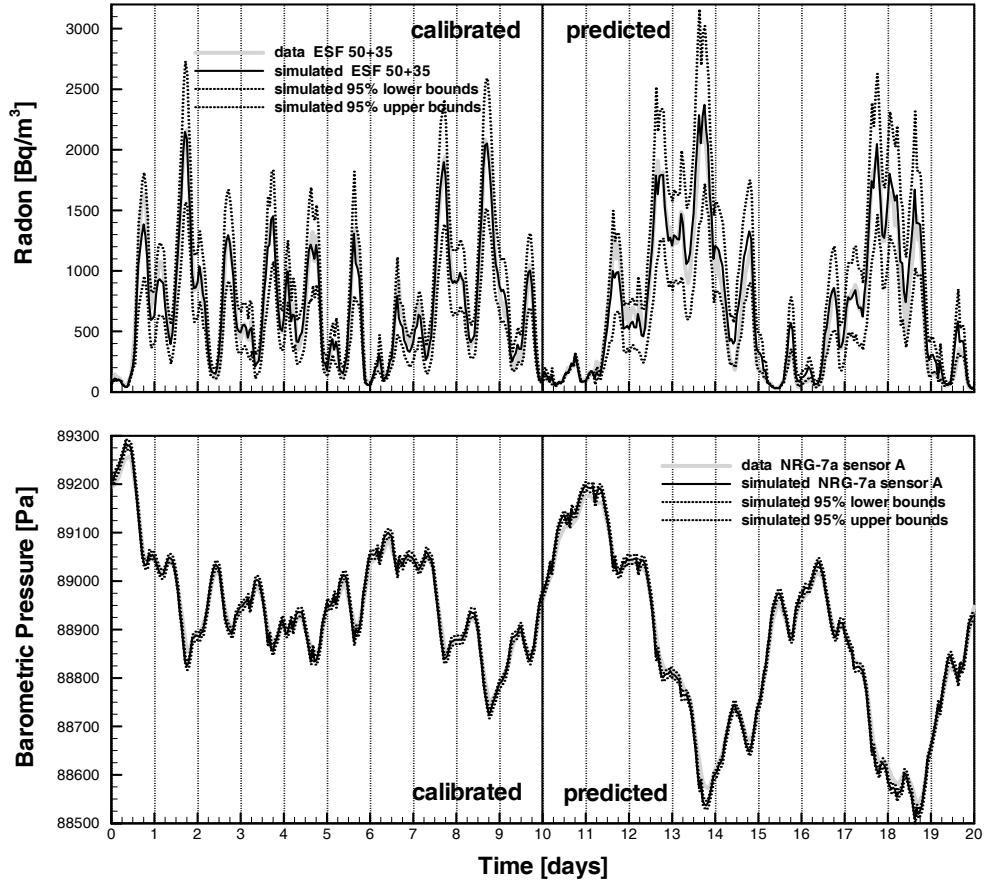


Figure 5. Model calibration and prediction results for radon concentrations at ESF 50+35, as well as gas-phase pressure fluctuations at borehole NRG-7a sensor A.

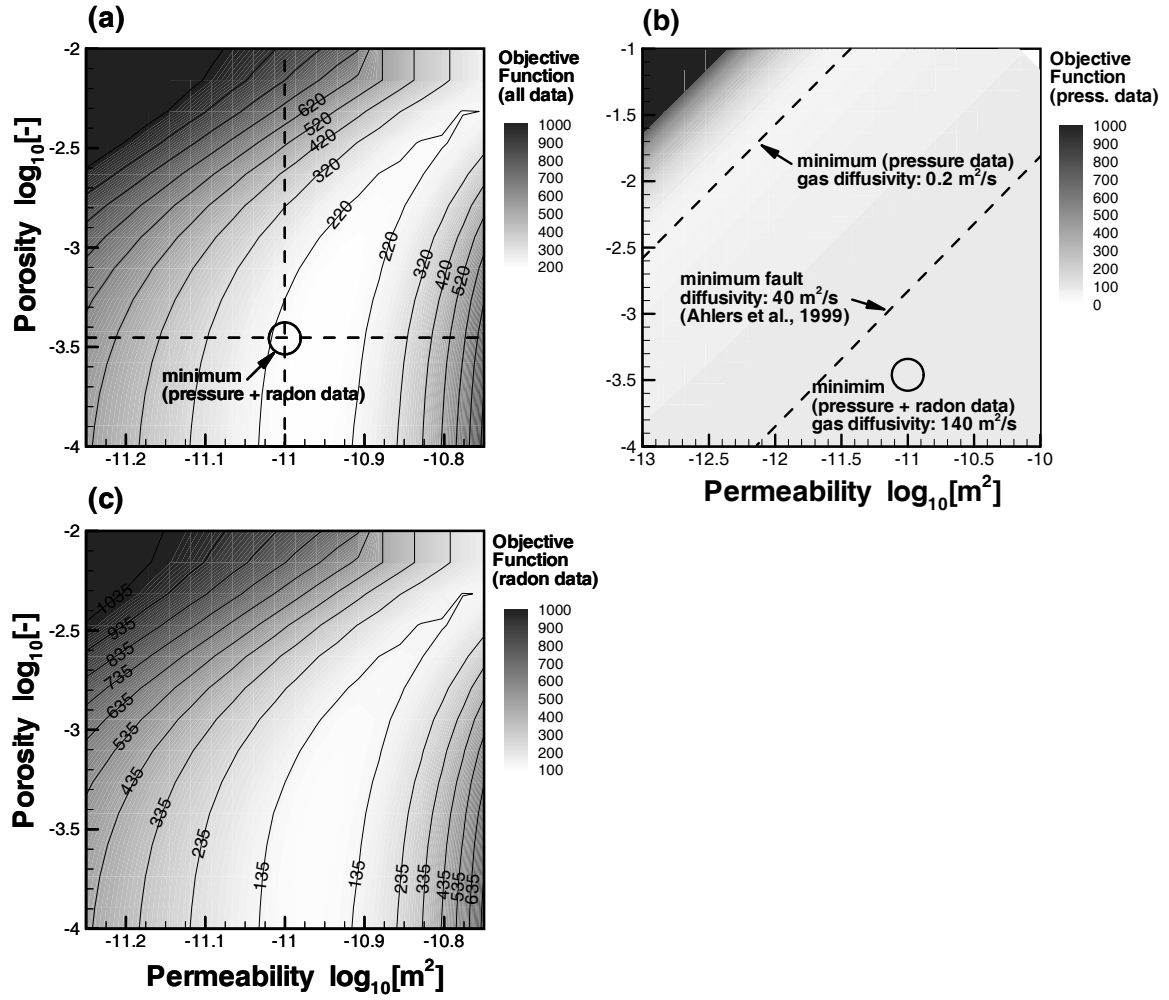


Figure 6. Objective function defined by the TSW fracture permeability and porosity when (a) both radon and pressure data are considered during calibration, (b) only pressure data are used, and (c) only radon data are used.

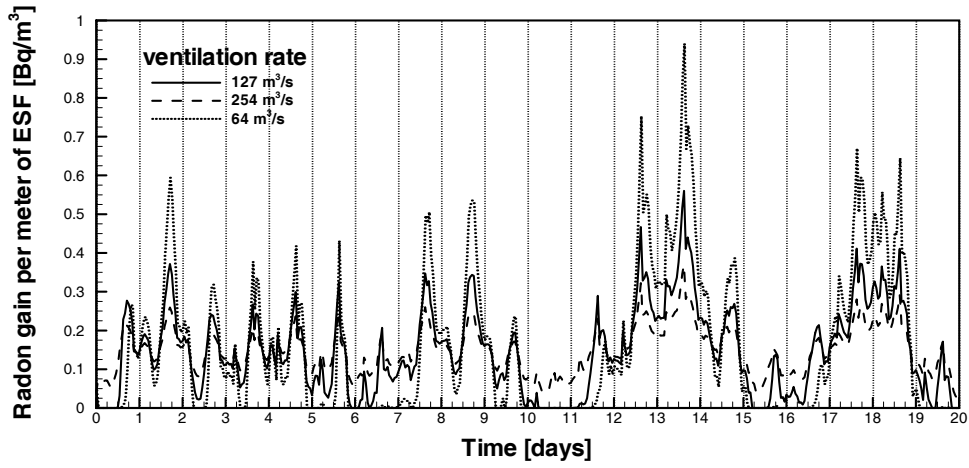


Figure 7. Gain in radon concentration per meter of ESF, calculated using three different ventilation rates.

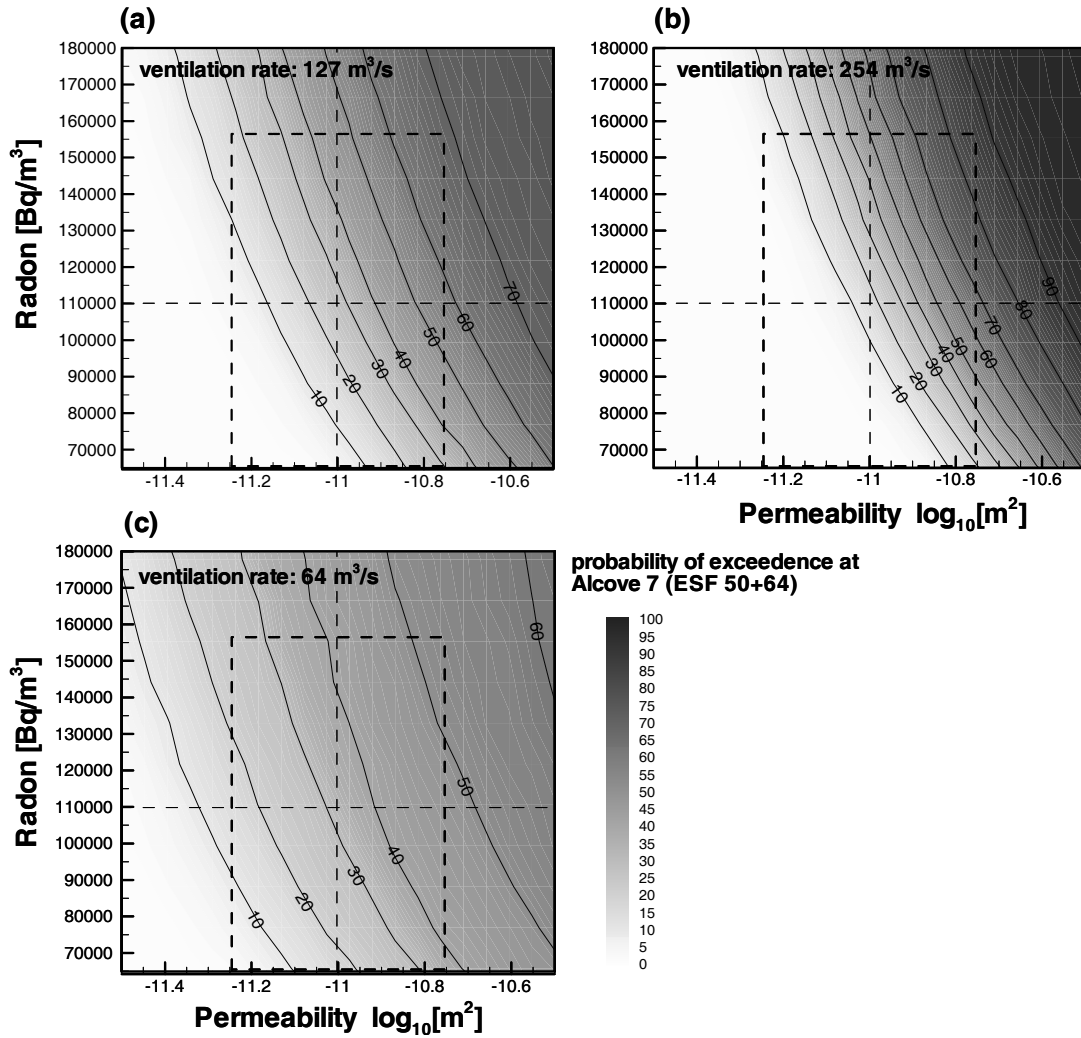


Figure 8. Probability of exceedence (for the 10 CFR Part 20 derived air concentration of radon) at Alcove 7 as a function of uncertainty in TSw fracture permeability and ambient radon concentration, using three different ventilation rates.